Numerical Study of the Effects of Gas Diffusion on Bubble Distribution about a Lifting Surface

Chao-Tsung Hsiao, Jingsen Ma, Georges L. Chahine

DYNAFLOW, INC., Jessup, Maryland, USA

ABSTRACT

Observations show that a large number of visible fine bubbles are present downstream of a cavitating lifting surface even in the absence of visible bubbles upstream. These bubbles propagate far downstream and can act as tracers of the body motion. To understand these observations, we consider numerically the flow field about a lifting surface accounting for bubble nuclei present in the liquid as well as nucleation from rigid boundaries. An Eulerian-Lagrangian model is used to obtain resolved descriptions of both the unsteady viscous flow field about the foil and the dynamics of a large number of bubble nuclei. Gas diffusion is included in the dynamics and is seen to play an important role on the resulting bubble nuclei size downstream. Bubble explosive growth and collapse is seen to be an essential 'catalyst' to enable significant gas diffusion and the bubble size becomes larger and visible downstream of the lifting surface due to a net influx into the bubble of gas originally dissolved in the liquid. Influx and outflux of vapor, which occur at a much faster rate, do not modify the final bubble size downstream. In addition to the gas diffusion, the effects of boundary nucleation and bubble breakup on the bubble size distribution are investigated.

Keywords

Gas Diffusion, Bubble Dynamics, Cavitation, Two-Phase Flow, Eulerian-Lagrangian Approach

1 INTRODUCTION

The interaction of a propeller and a bubbly medium is of relevance to many engineering problems since all waters, including supposedly pure waters, contain microscopic bubble nuclei and are actually two-phase media. The interaction affects both the lifting surface performance and the bubbly flow characteristics.

Even in the absence of visible upstream bubbles, photographic evidence has shown that a relatively large amount of bubbles is generated downstream of a propeller.

Cavitation initiates at weak spots of the liquid or nuclei; i.e. very small microscopic bubbles, particles with crevices in suspension in the liquid, or entrapped gaseous micro- or nano-bubbles at the rigid boundaries. The established presence of such nuclei in the ocean and in cavitation tunnels has been quantified during campaigns through various measurement techniques (e.g. Billet, 1985, Wu & Chahine, 2010). Bubble size distributions in the ocean depend on the geographical location, the environmental conditions, the season, the time of the day, and the depth. In cavitation tunnels, it depends on the presence in the facility of desorbers, seeders, or bubble nuclei controllers, and on the duration of operation of these prior to the tests.

Therefore, it is essential that the analysis of bubble distributions and dynamics and their effects on propeller behavior starts from the consideration of the presence of an initially prescribed bubble size distribution (BSD). These initial bubble nuclei, when subjected to variations in the local liquid pressures (e.g. when flowing over a lifting), will respond dynamically by changing volume, oscillating, and eventually switching from being sub-visual to becoming visible due to local explosive growth, collapse, splitting, and cumulative gas transfer into the bubbles ("rectified" diffusion).

In this paper, we extend our previous study on the effects of a propeller on bubble size distribution (Hsiao & Chahine 2012) to the unsteady flow over a lifting surface. We consider an Eulerian-Lagrangian approach with the foil flow field solved in an Eulerian frame, while the bubbles are tracked in a Lagrangian frame. The study includes consideration of the diffusion of dissolved non-condensable gas in the liquid and gas transfer at the gas-liquid interfaces. It also considers the effects of nucleation from the surface of the foil and of bubble breakup during strong bubble dynamics, on the downstream bubble size distribution.

2 Numerical Models

2.1 Eulerian-Lagrangian Approach

The Eulerian-Lagrangian two-phase flow framework employed in this study has been extensively applied and documented in our previous studies. These include modeling of propeller tip vortex cavitation inception (Hsiao & Chahine 2004, Hsiao & Chahine 2008), investigations of the effects of a propeller flow on bubble size distribution in water (Hsiao & Chahine 2012), bubble entrainment in plunging jets (Hsiao et al. 2013) and wave propagation in bubbly media and bubble cloud collapse studies (Raju et al. 2011; Ma et al. 2015a; Ma et al. 2015b). The general procedure includes the following main steps:

1. The dynamics and motion of the individual bubbles in the flow field are controlled by the two-phase medium local properties and gradients.
2. The local properties of the mixture (void fractions and local densities) are determined by the instantaneous bubble sizes and distribution.
3. The mixture flow field has an evolving density distribution, which is space and time dependent, and satisfies mass and momentum conservation.

The approach allows two-way coupling between the continuum-based model and the discrete bubbles model.

2.2 Eulerian Continuum-Based Mixture Model

The two-phase flow continuum model uses the Navier-Stokes equations solver, 3DYNAFS-VIS$^©$, to satisfy the continuity and momentum equations:

$$\frac{\partial \rho_m}{\partial t} + \nabla \cdot \left(\rho_m \mathbf{u} \right) = 0, \tag{1}$$

$$\rho_m \frac{D\mathbf{u}}{Dt} = -\nabla p + \mu_m \nabla^2 \mathbf{u}, \tag{2}$$

where the subscript m represents the mixture properties. $\mathbf{u}$ is the mixture velocity and p is the pressure. The mixture density, ρ_m, and the mixture viscosity, μ_m, can be expressed as functions of the bubble (gas and vapor) volume fraction, α, by:

$$\rho_m = \left(1 - \alpha\right)\rho_l + \alpha\rho_g, \quad \mu_m = \left(1 - \alpha\right)\mu_l + \alpha\mu_g, \tag{3}$$

where the subscript l represents the liquid and the subscript g represents the gas. The medium density and viscosity are time- and space-dependent.

The system of equations is solved by an artificial compressibility method (Chorin, 1967) in which a pseudo-time, τ, derivative of the pressure multiplied by the artificial compressibility factor, β, is added to the continuity equation as:

$$\frac{1}{\beta} \frac{\partial p}{\partial \tau} + \frac{\partial \rho_m}{\partial t} + \nabla \cdot \left(\rho_m \mathbf{u} \right) = 0. \tag{4}$$

As a consequence, a hyperbolic system of equations is formed and can be solved using a time marching scheme. The solution is iterated in the pseudo-time until convergence. To obtain a time-dependent solution, a Newton iterative procedure is performed at each physical time step in order to satisfy the continuity equation.

2.3 Lagrangian Discrete Bubble Model

The Lagrangian discrete bubble model, 3DYNAFS-DSM$^©$, uses singularities to model the bubbles. Averaging over the bubble surface is applied to the local fluid quantities (Hsiao et al., 2003, Chahine, 2004, Choi et al., 2004). This model has been shown to produce accurate results when compared to full 3D two-way interaction computations (Hsiao and Chahine 2003). The source terms, representing bubble volume oscillations, use a Surface Averaged Pressure (SAP) modified version of the Keller-Herring equation (Keller and Kolodner, 1954) to describe the bubble dynamics (Ma et al. 2015b),

$$\left(1 - \frac{\dot{R}}{c_m}\right)R\ddot{R} + \frac{3}{2}(1 - \frac{\dot{R}}{3c_m})\dot{R} = \frac{\mathbf{u}_s^2}{4} +$$

$$\frac{1}{\rho_m}\left(1 + \frac{\dot{R}}{c_m} + \frac{R}{c_m}\frac{d}{dt}\right) \cdot \tag{5}$$

$$\left[p_v + p_g - p_{enc} - \frac{2\gamma}{R} - 4\mu_m \frac{\dot{R}}{R}\right].$$

where c_m is the local sound speed in the mixture. R is the bubble radius at times t, p_v is the liquid vapor pressure, and $\mathbf{u}_{enc}$ and p_{enc}, are respectively the averages of the liquid velocities and pressures over the bubble surface. The slip velocity, $\mathbf{u}_s = \mathbf{u}_{enc} - \mathbf{u}_b$ is the difference between $\mathbf{u}_{enc}$ and the bubble translation velocity, $\mathbf{u}_b$. The gas pressure, p_g, is obtained from a polytropic compression law if no gas mass transfer effects are included. When gas diffusion is included, the gas pressure is obtained from the solution of the gas diffusion problem and energy balance.

The bubble trajectory is obtained from the following bubble motion equation:

$$\frac{d\mathbf{u}_b}{dt} = \left(\frac{\rho_l}{\rho_g}\right)\left[\frac{3}{8R}C_D|\mathbf{u}_s||\mathbf{u}_s| + \frac{1}{2}\left(\frac{d\mathbf{u}_{enc}}{dt} - \frac{d\mathbf{u}_b}{dt}\right) + \right.$$

$$\left. \frac{3\dot{R}}{2R}\mathbf{u}_s - \frac{\nabla p}{\rho_l} + \frac{(\rho_b - \rho_l)}{\rho_l}g + \frac{3C_L}{4\pi}\frac{\sqrt{\nu}}{R}\frac{\mathbf{u}_s \times \mathbf{\Omega}}{\sqrt{|\mathbf{\Omega}|}}\right], \tag{6}$$

where C_D is the bubble drag coefficient, given by an empirical equation, such as from Haberman and Morton (1953). C_L is a lift coefficient and Ω is the vorticity vector. The 1st right hand side term is a drag force. The 2nd and 3rd terms account for the added mass. The 4th term accounts for the presence of a pressure gradient, while the 5th term accounts for gravity and the 6th term is a lift force (Saffman 1965).

2.4 Gas Diffusion Model

Liquids contain non-condensable gas not only in a suspended form (bubbles, nuclei) but also in a dissolved form with a concentration C. In the absence of dynamics, this results from equilibrium at the gas-liquid interfaces. In the presence of a local concentration gradient, dissolved non-condensable gas will diffuse from the high concentration region to the low concentration region. The transport equation for the time and space dependent dissolved non-condensable gas concentration in the liquid is given by:

$$\frac{\partial C}{\partial t} + \mathbf{u} \cdot \nabla C = D_g \nabla^2 C, \tag{7}$$

where D_g is the molar diffusivity of the gas in the liquid (Hsiao & Chahine 2012).

At a bubble interface, the dissolved gas concentration, C_s, is connected to the gas pressure, p_g, through Henry's law:

$$C = C_s \text{ at } r = R \text{ with } C_s = \frac{p_g}{H}, \tag{8}$$

where H is the Henry constant. This condition at the bubble interface is very important and actually drives the gas

diffusion dynamics. The other initial and boundary conditions for gas diffusion are:

$$C = C_\infty \quad \text{for } t = t_0,$$
$$C \to C_\infty \quad \text{for } r \to \infty, \tag{9}$$

where C_∞ is the dissolved gas concentration far away from the bubble surface.

The gas transfer rate, $\dot{n}_g$, at the bubble/liquid interface, is directly proportional to the interfacial area and the normal concentration gradient at the interface,

$$\dot{n}_g = D_g \int_S \frac{\partial C}{\partial n} dS. \tag{10}$$

2.5 Model Closure

To obtain the gas pressure inside the bubble when gas diffusion is taken into account, we consider the instantaneous energy and mass balance of the bubble content. Both components of the bubble content, vapor and gas, are assumed to be ideal gases, which follow the ideal gas law:

$$\left(p_g + p_v\right)V_b = \left(n_g + n_v\right)R_u T_b, \tag{11}$$

where V_b is the volume of bubble, n_g is the number of moles of gas within the bubble, n_v is the number of moles of vapor, R_u is the universal gas constant and T_b is the absolute temperature of the gas and vapor mixture. One consequence of this assumption is that the amount of n_g and n_v in the bubble are directly proportional to the ratio of their respective partial pressures.

Due to the relatively short vaporization time compared to bubble dynamics and gas diffusion characteristic times, the vapor is considered to instantaneously flow in and out of the bubble, and p_v is assumed equal to the equilibrium vapor pressure of the liquid at the bubble wall temperature.

Considering the thermodynamics of the contents of the bubble and applying the first law, the energy balance for the control volume bounded by the bubble surface is

$$dU = -dW + \sum_{i=v,g} \dot{n}_i\, h_i\, dt, \tag{12}$$

where dU is the change in internal energy, dW is the work done on the control volume, and h_i is the specific enthalpy of constituent i. The terms can be expanded as:

$$dU = \sum_{i=v,g} c_{V,i}\, d(n_i T_b),$$
$$dW = (p_v + p_g)\, dV_b, \tag{13}$$
$$h_i = \sum_{i=v,g} c_{P,i}\, T_l,$$

where c_V is the specific heat at constant volume, c_P is the specific heat at constant pressure and T_l is the liquid temperature. Combining Eq. (11), (12) and (13), and using superscripts T_b and T_l for c_V and c_P to indicate whether the specific heats are evaluated at corresponding bubble or liquid temperature we obtain:

$$c_{V,v}^{T_b} \frac{p_v \dot{V}_b}{R_u} + c_{V,g}^{T_b} \frac{\left(\dot{p}_g V_b + p_g \dot{V}_b\right)}{R_u} + \left(p_v + p_g\right)\dot{V}_b$$
$$- c_{P,v}^{T_l} T_l \frac{p_v}{p_g}\dot{n}_g + c_{P,v}^{T_l} T_l \frac{p_v \dot{p}_g}{p_g^2} n_g - \dot{n}_g c_{P,g}^{T_l} T_l = 0. \tag{14}$$

Using the fact that $c_P - c_V = R_u$, Eq. (14) becomes:

$$\dot{p}_g = \frac{E / p_g - D p_g - F}{A + B / p_g^2},$$

$$A = \left(c_{P,g}^{T_b} - R_u\right)\frac{V_b}{R_u}, \qquad B = c_{P,v}^{T_l} T_l p_v n_g,$$

$$D = c_{P,g}^{T_b} \frac{\dot{V}_b}{R_u}, \qquad E = c_{P,v}^{T_l} T_l p_v \dot{n}_g, \tag{15}$$

$$F = \frac{c_{P,v}^{T_b}}{R_u} p_v \dot{V}_b - c_{P,g}^{T_l} T_l \dot{n}_g.$$

Integration of Eq. (15) provides the instantaneous gas pressure to be used in Eq. (5) and Eq. (8).

2.6 Numerical Solution for Gas Diffusion Equation

To solve the gas diffusion equation one can use the thin boundary layer approach introduced by Plesset and Zwick (1952). Although this approach enables a good analytical solution for Eq. (8), it requires integration over the whole history of the bubble dynamics in order to accurately compute the amount of gas inside the bubble:

$$C_s = C_\infty - \left(\frac{D_g}{\pi}\right)^{1/2} \int_0^t \frac{\dot{n}_g}{\left[\int_\tau^t R^4(y)dy\right]^{1/2}} d\tau. \tag{16}$$

Using this approach requires too much computer memory when the considered number of bubbles is large. In this case, a direct numerical solution of the diffusion equation is more affordable. A finite difference method to solve Eq. (8) was instead implemented after transforming, for a spherical problem, Eq. (7) using the moving coordinate system, ξ,

$$\frac{\partial C}{\partial \tau} = D_g \frac{\partial}{\partial \xi}\left(r^4 \frac{\partial C}{\partial \xi}\right), \quad \text{with} \quad \xi = \frac{1}{3}\left(r^3 - R^3\right). \tag{17}$$

This coordinate transform simplifies the solution by removing the convection term.
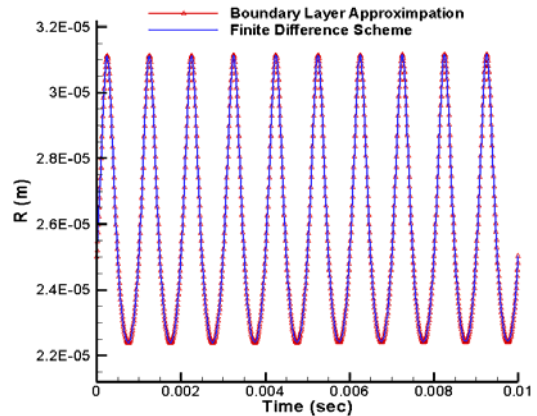

Figure 1. Comparison of bubble radius between the thin boundary layer approach and the finite difference method.

For validation, Figure 1 shows a comparison of the time history of the bubble radius between the thin-boundary layer approach and the finite difference method for a bubble excited by a sinusoidal acoustic wave. The comparison shows good agreement with only 21 grid points for the finite difference method.

3 RESULTS AND DISCUSSION

3.1 Unsteady Single Phase Flow
The present study considers, in the presence of natural nuclei, the unsteady flow field over a NACA0015 finite-span rectangular hydrofoil with a round tip and an aspect ratio based on semi-span of 2. The computational domain has all far-field boundaries located six chord lengths away from the foil and is discretized using an H-H type grid with a total of 2.1 million grid points (191×111×101). 121×81 grid points are used to discretize the foil surface. The first grid above the hydrofoil surface is at $y^+=1$ in order to properly describe the boundary layer.

We consider an incoming uniform flow at an angle of attack of 4°. Freestream velocities and pressures are specified in the far-field side boundaries and in the inflow boundary, while a first order extrapolation for all variables is used at the outflow boundary. A symmetry boundary condition is applied at the foil root section and no-slip flow and zero normal pressure gradient conditions are imposed on the foil surface. The flow is directly simulated without a turbulence model at a Reynold number Re=1.5x10^6 (chord length C_l= 0.15 m and liquid velocity U_∞= 10 m/s). In the absence of nuclei, unsteady flow separation with vortex shedding is observed in the liquid and the computations are conducted until limit cycle oscillations are reached. Figure 2 shows the non-dimensional pressure contours over the blade surface, $(p-p_\infty)/\rho V_\infty^2$, over which is superposed in grey the 3D iso-surface of the pressure -0.5 at a selected time after reaching limit cycle oscillations.
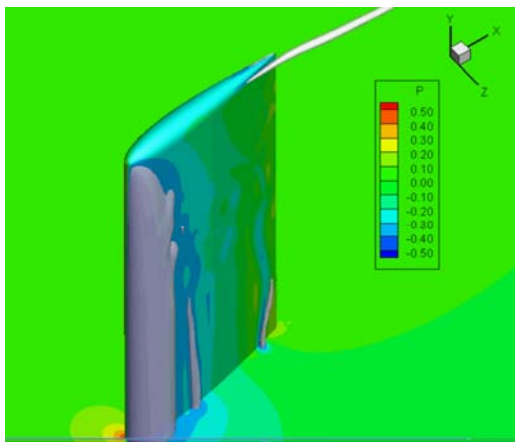

Figure 2. Non-dimensional pressure contours and iso-surface of pressure at level of -0.5 shown at a selected time after reaching limited cycle oscillations (i.e. converged solution but oscillating in time).

3.1 Dispersed Bubbly Flow
To study the interaction between nuclei and the foil, 90,000 free field bubble nuclei with radii ranging from 20 to 60 μm are released from a preset release domain of dimensions 0.15×0.32×0.04m^3 upstream of the foil. This corresponds to an average void fraction of 1×10^{-6} in the release domain. Figure 3 shows the resulting bubble distribution in the field before considering gas diffusion effects, for a cavitation number, σ = 1.0. We can observe that the nuclei grow to large sizes in the low-pressure regions over the foil, i.e. on the suction side near the leading edge and in the tip vortex region. However, the bubbles return to their original size once the field pressure returns to a value similar to the upstream pressure.
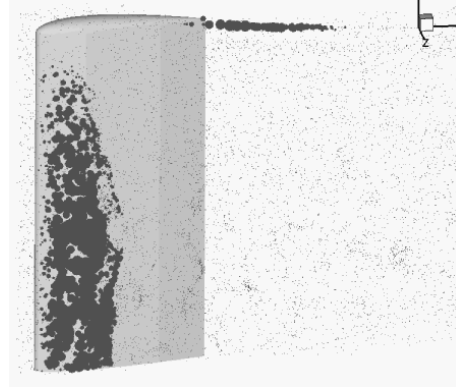

Figure 3. Bubble distribution over the foil shown at a selected time when gas diffusion effects are not taken into account.

3.3 Gas Diffusion Effects
Gas diffusion effects on the results are then considered when the water is assumed to be supersaturated (i.e. with a dissolved gas concentration of 100%, or 0.66 mol/m^3 of dissolved air). Figure 4 shows the resulting bubble distribution. Here, we see a similar behavior to that in the absence of gas diffusion during the bubble growth phase. However, significant differences are observed in the wake region after the bubbles start collapsing and rebounding. The bubbles retain much larger sizes and the fine vortices in the wake are made visible due to the collected larger bubbles. Such a phenomenon is also observed in the experimental study by de Graaf et al. (2014).
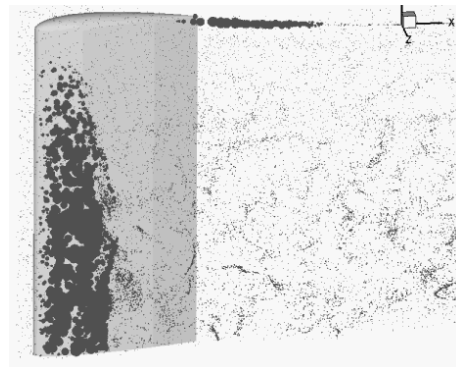

Figure 4. Bubble size distribution over the finite-span hydrofoil shown at a selected time when diffusion is taken into consideration.

To illustrate quantitatively the effects of the foil presence and of gas diffusion on the bubble nuclei as they pass over the finite-span hydrofoil, we integrate the volume of all bubbles in the interrogation volume shown in Figure 5. The volume includes the full height in the z direction and has a width, Δy=0.32 m, and a thickness, Δx=0.01m.
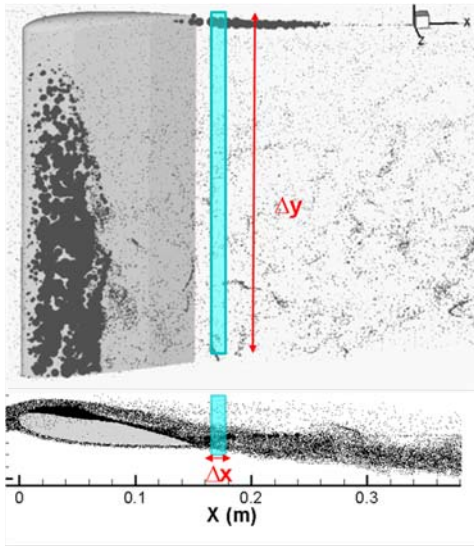

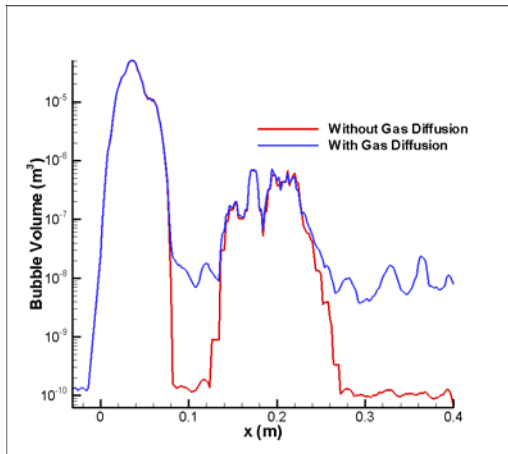**Figure 5. Illustration of the interrogation volume for bubble volume and size analysis.**

Figure 6. Total bubble volume in the interrogation volume. Comparison of results with and without gas diffusion effects.

Figure 6 shows the variation of the total volume of bubbles in the moving strip ($\Delta x, \Delta y$) in the stream wise direction, and compares the results between the cases where gas diffusion effects are considered or ignored. Between $x \simeq -0.02m$ and $x \simeq 0.08m$ the bubble volume increases dramatically by almost six orders of magnitude due to cavitation on the foil suction side. In this region, the effects of gas diffusion are not visible. This is followed by the bubble collapse and successive rebounds and oscillations for $x > 0.08m$. In this region, the total bubble volume with gas diffusion is seen to be two order of magnitude larger than that in the absence of gas diffusion. This effect is less visible between $x \simeq 0.14m$ and $x \simeq 0.25m$ due to the growth of bubbles captured in the tip vortex flow region.

Figure 7 shows a comparison of the bubble size distribution at x=0.4m. It is seen that, while in the absence of gas diffusion, the bubbles sizes return to the initial 20 μm, 40 μm and 60 μm, in the presence of gas diffusion, foil cavitation significantly modifies the size of the downstream nuclei distributing them widely between 20 μm and 300 μm.
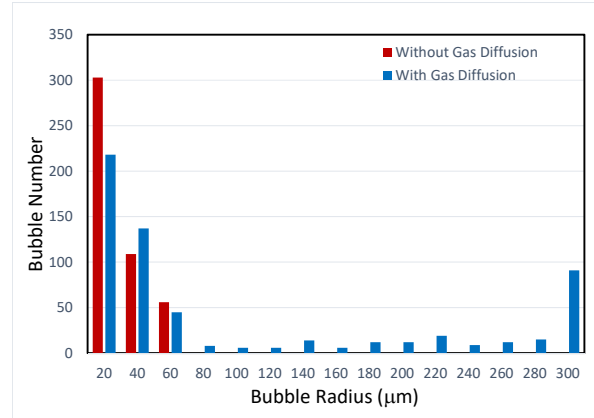

Figure 7. Comparison of bubble size distribution at x=0.4m between considering and ignoring gas diffusion effects.

3.4 Effect of Boundary Nucleation

A boundary nucleation model based on existing experimental observations and theoretical studies was introduced by Hsiao et al (2017) to model the initiation and dynamics of sheet cavitation on foils. In the nucleation model, nuclei are released from rigid boundaries cells when the pressure at the cell center drops below a threshold pressure, e.g. the vapor pressure. N nuclei are then released from the cell in the flow field during the time interval Δt:

$$N = N_s f_n \Delta t \Delta A , \qquad (18)$$

where N_s is the number density of nucleation sites per unit area, ΔA is the cell surface area, and f_n is the emission rate.

The boundary nucleation model was found to recover very well experimentally measured (Berntsen et al. 2001) time-averaged cavity length and oscillation frequency (Hsiao et al, 2017).
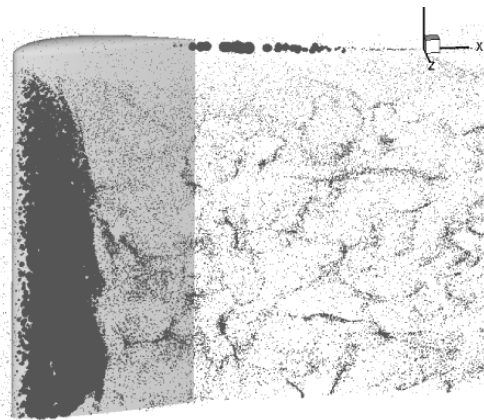

Figure 8. Bubble distribution over the finite-span hydrofoil shown at a selected time with both free nuclei and boundary nucleation model (f_n =0.8 kHz and N_s =10 cm⁻²).

We consider this model here to investigate the effects wall nucleation have on the bubble distribution downstream of the foil. Figure 8 shows the resulting bubble distribution with both field nuclei and boundary nucleation present. It is seen that the density of bubbles is higher in the lower pressure region near the leading edge where the boundary nucleation is active (Figure 9). This has, however, little effect on bubble volume in the tip vortex because the wall nuclei do not reach the tip vortex region. Finally, in the wake region, the number of larger-sized bubbles obtained from both nuclei sources is much higher than that obtained from the free nuclei only as seen in Figure 10.
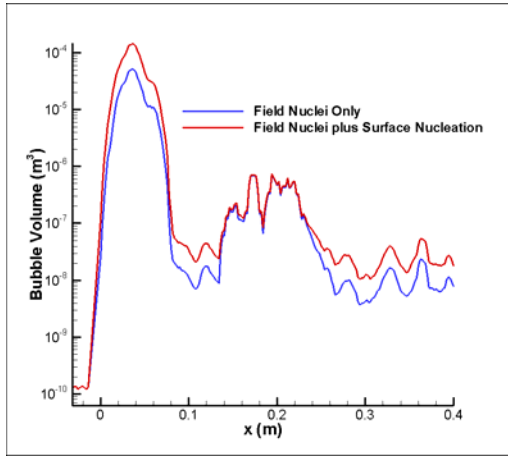

Figure 9. Comparison of bubble volume variation along the stream wise direction between the simulations with free nuclei only and with both free and surface nuclei.
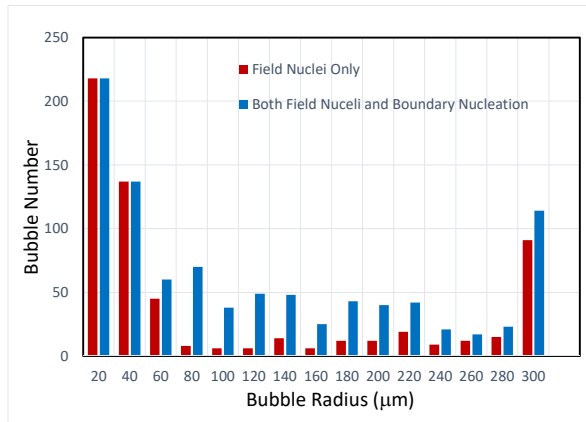

Figure 10. Comparison of bubble size distribution at x=0.4m between the simulations with free nuclei only and the one with both nuclei sources.

3.5 Non-spherical Bubble Simulation

To gain more insight into bubble dynamics and breakup on the hydrofoil, a 3D simulation of a traveling cavitation bubble very close to the foil surface, its 3D deformation, and its breakup into multiple smaller bubbles is conducted. The setup is the same as in the above simulations, with the exception that a finite thickness of 0.1 chord length is considered in the span direction with periodic boundary conditions imposed at both sides.

As shown in Figure 11, a small bubble is released near the leading edge. As it travels into the low-pressure region on the suction side of foil, it grows, strongly deforms, then breaks up into a multiple of small bubbles while it travels further downstream and encounters higher pressures and shear flow near the foil boundary.

This is further highlighted in Figure 12, which displays a sequence of zoomed front views of the bubble interacting with the liquid flow around it. From this figure it is seen, that the bubble elongates in the streamwise direction due to the foil viscous shear flow. A reverse flow is also seen under the bubble, particularly near its leading edge (a). This reverse flow creates local vorticity, which in turn shears off the downstream bubble part (b & c), introducing a strong secondary flow under the bubble (d). This local disturbance then further breaks up the bubble.

This preliminary simulation implies the important role played by the local vorticity and shows bubble-induced flow disturbance during the bubble dynamics and breakup. In on-going studies the simulations will be refined with the ultimate goal of uncovering breakup criteria to correlate the breakup parameters with local flow conditions such as vorticity and turbulence, etc.
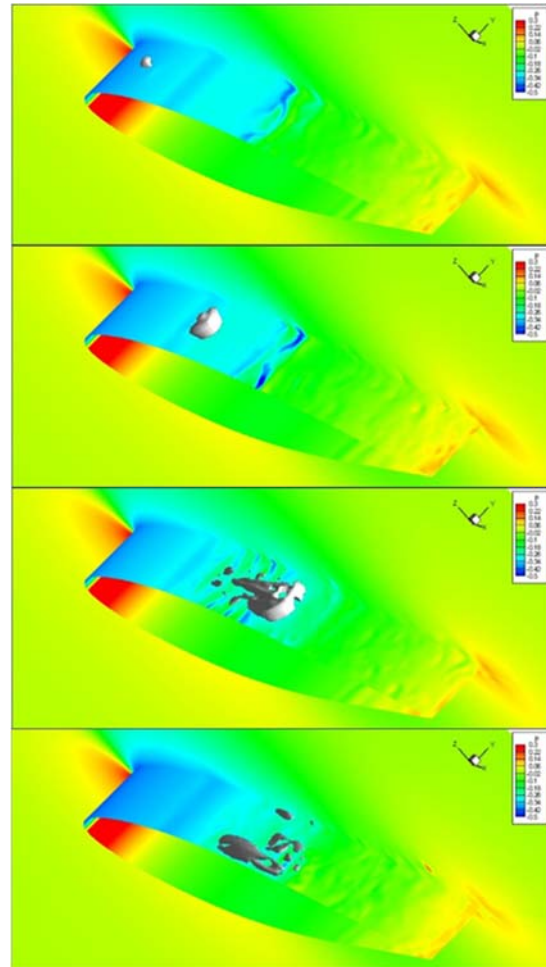

Figure 11. 3D simulation of a non-spherical traveling cavitation bubble on a NACA0015 foil, where the silver iso-surface represents the bubble gas/liquid interface and the background flow is contoured by flow pressure.
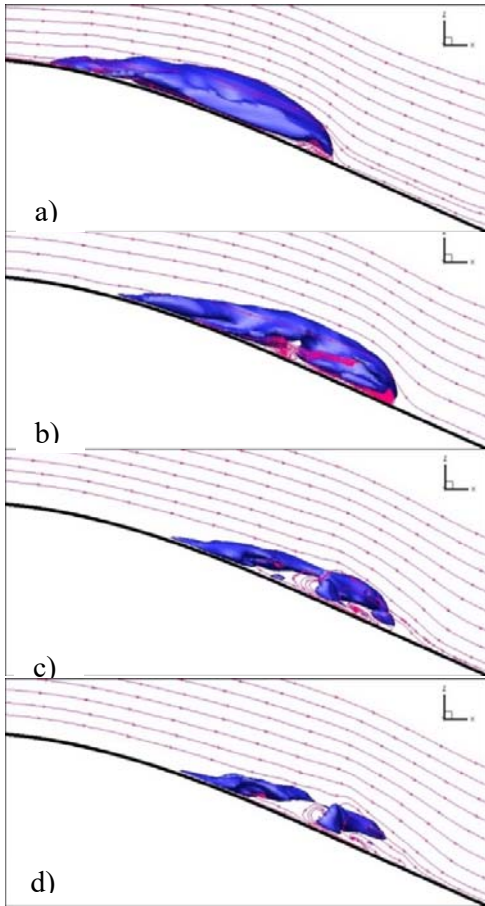
a)

b)

c)

d)

Figure 12. A time sequence of the bubble interacting with the liquid flow around it, where the blue iso-surface represents the 3D bubble surface and the purple lines are streamlines in the central plane of domain

3.6 Effect of Bubble Breakup

The above study has shown that the bubble may break up into multiple "daughter" bubbles when it collapses and rebounds. Early theoretical studies by Plesset and his coworkers also showed that the bubble becomes highly unstable to nonspherical disturbances during bubble rebound due to Taylor instability.

In the absence of a physically established model for bubble breakup in pressure gradients and near boundaries, we investigate here the effects of bubble breakup using a heuristic model with the following characteristic parameters: breakup threshold, breakup moment, number of daughter bubbles, sizes of daughter bubbles, and locations of daughter bubbles. We impose that the total volume and the amount of non-condensable gas in the daughter bubbles remain the same as in the mother bubble after breakup. We also apply the breakup model only to strongly collapsing bubbles, i.e. for bubbles where the ratio of maximum bubble radius to initial minimum radius exceed a given threshold (here we used 20) and assume the breakup moment to be at the time of rebound. The number, sizes, and locations of daughter bubbles are selected

arbitrarily as being 4 bubbles of equal size located within the confines of the mother bubble.

Figure 13 shows the resulting dispersed bubbles when the bubble breakup model is applied and only free nuclei are considered. By comparing to Figure 4, we can see significant differences in the wake region, downstream of the bubble collapse region, downstream of which bubbles break up at rebound. Comparison of bubble volumes in Figure 14 does not show major influence of breakup on the total volumes because of the condition imposed of volume conservation at breakup. However, the bubble size distribution in the wake region is significantly different between the two cases. As can be seen in Figure 15, the breakup model significantly alters the bubble size distribution at x=0.4m. including bubble breakup results in a significant increase in the number of small and mid-size bubbles and a reduction in the large size bubbles.
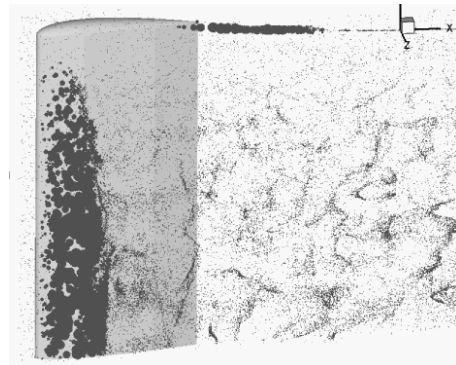

Figure 13. Bubble size distribution over the finite-span hydrofoil shown at a selected time when diffusion and bubble break up are taken into consideration.
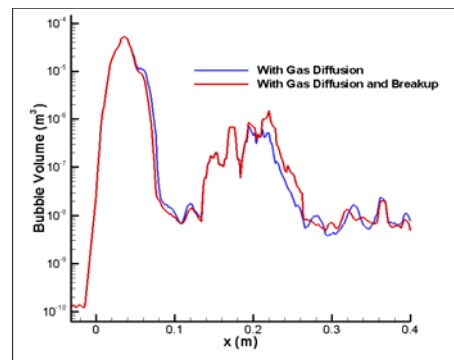

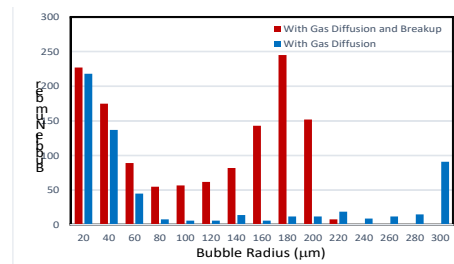**Figure 14. Comparison of the streamwise bubble volume distribution with and without bubble breakup.**

Figure 15. Comparison of bubble size distribution at x=0.4m between the simulations with and without considering bubble breakup.

4 CONCLUSIONS

An Eulerian-Lagrangian model is used to simulate a dispersed bubble flow over a finite-span rectangular hydrofoil. A gas diffusion model is implemented and complements the dynamics of traveling cavitation bubbles in the unsteady flow field. Inclusion of gas diffusion in the model significantly alters the behavior of the bubbles in the wake after they collapse and rebound and results in much larger bubbles. This makes the fine vortices in the wake visible due to the collected larger bubbles. Inclusion of boundary nucleation also significantly increases the number of larger bubbles in the wake.

Finally, including non-spherical effects shows that the bubbles are sheared and break up into several smaller bubbles. Inclusion of bubble breakup in the overall model results in a significant increase in the number of small and mid-size bubbles and a reduction in the large size bubbles.

REFERENCES

Berntsen, G.S., M. Kjeldsen, and R.E. Arndt. "Numerical Modeling of Sheet and Tip Vortex Cavitation with FLUENT 5," in Fourth International Symposium on Cavitation. Pasadena, CA, 2001.

Billet, M. L. "Cavitation nuclei measurements – a review," ASME Cavitation and Multiphase Flow Forum," FED Vol 23, June 1985.

Chahine, G.L., "Nuclei Effects on Cavitation Inception and Noise", Keynote presentation, 25th Symposium on Naval Hydrodynamics, St. John's, Newfoundland, Canada, Aug. 8-13, 2004.

Chorin, A.J., "A Numerical Method for Solving Incompressible Viscous Flow Problems," Journal of Computational Physics, **2**, pp. 12-26, 1967.

Choi, J.-K., Hsiao, C.-T., and Chahine, G.L., "Tip Vortex Cavitation Inception Study Using the Surface Averaged Pressure (SAP) Model Combined with a Bubble Splitting Model", 25th Symposium on Naval Hydrodynamics, St. John's, NL, Canada, 2004.

de Graaf, K.L., Zarruk, GA, Brandner, P.A. and Pearce, B.W. (2014), Microbubble content in the wake of a cavitating hydrofoil, 19th Australasian Fluid Mechanics Conference, Melbourne, Australia.

Haberman, W.L., Morton, R.K., "An Experimental Investigation of the Drag and Shape of Air Bubbles Rising in Various Liquids," Report 802, DTMB, 1953.

Hsiao, C.-T., Chahine, G. L., and Liu, H.-L., "Scaling Effects on Prediction of Cavitation Inception in a Line Vortex Flow", Journal of Fluids Engineering, **125**, pp.53-60, 2003.

Hsiao, C.-T., Chahine, G.L., "Prediction of Vortex Cavitation Inception Using Coupled Spherical and Non-Spherical Models and Navier-Stokes Computations," Journal of Marine Science and Technology, **8**, No. 3, pp. 99-108, 2004.

Hsiao, C.-T. and Chahine, G.L., "Tip Vortex Cavitation Inception Scaling for an Open Marine Propeller," 27th Symposium on Naval Hydrodynamics, Rome, Korea, October 5-10, 2008.

Hsiao, C.-T., and Chahine, G.L. "Effect of a propeller and gas diffusion on bubble nuclei distribution in a liquid", Journal of Hydrodynamics, Ser B, Vol. 24 (6), pp. 809-822, 2012.

Hsiao, C.T., Wu, X., Ma, J., and Chahine, G.L. "Numerical and experimental study of bubble entrainment due to a horizontal plunging jet", International Shipbuilding Progress, Vol. 60, (1), pp. 435-469, 2013.

Hsiao, C.-T., Ma, J., Chahine, G.L. "Multiscale Two-Phase Flow Modeling of Sheet and Cloud Cavitation", International Journal of Multiphase Flow, Vol. 90, pp. 102-117, 2017.

Keller, J. B., and Kolodner. I., "Instability of liquid surfaces and the formation of drops", Journal of Applied Physics, Vol 25(7) , pp. 918-921, 1954.

Ma, J., Hsiao, C.-T., Chahine, G.L. "Spherical Bubble Dynamics in a Bubbly Medium using an Euler-Lagrange Model Corresponding," Chemical Engineering Science, Vol 128, pp. 64-81, 2015a.

Ma, J., Hsiao, C.-T., Chahine, G.L. "Euler-Lagrange Simulations of Bubble Cloud Dynamics near a Wall", ASME Journal of Fluids Engineering, Vol. 137, (4), 041301, 2015b.

Plesset, M.S., Zwick, S.A., "A Non-Steady Heat Diffusion Problem with Spherical Symmetry," Journal of Applied Physics, **23** (1), pp. 95-98, 1952.

Raju, R., Singh, S., Hsiao, C.-T., and Chahine, G. "Study of Pressure Wave Propagation in a Two-Phase Bubbly Mixture", ASME Journal of Fluids Engineering, Vol. 133, (12), pp. 121302-1-121302-12, 2011.

Saffman, P. G., "The Lift on a Small Sphere in a Slow Shear Flow", Journal of Fluid Mechanics, **22**, 385-400, 1965.

Wu, X., Chahine, G. L. "Development of an acoustic instrument for bubble size distribution measurement," Journal of Hydrodynamics, Ser. B, Vol. 22 (5), pp 330-336, 2010.